

Highlights

Proper Orthogonal Descriptors for Multi-element Chemical Systems

Ngoc Cuong Nguyen

- Proper orthogonal descriptors are introduced for multi-element chemical systems.
- Two potentials are developed by using linear and quadratic expansions of the proper orthogonal descriptors.
- The potentials are demonstrated for indium phosphide and titanium dioxide.
- The quadratic potential is more accurate than the linear potential at the same cost.

Proper Orthogonal Descriptors for Multi-element Chemical Systems

Ngoc Cuong Nguyen^a

^a*Center for Computational Engineering, Department of Aeronautics and Astronautics,
Massachusetts Institute of Technology, 77 Massachusetts
Avenue, Cambridge, MA, 02139, USA*

Abstract

We introduce the proper orthogonal descriptors for efficient and accurate interatomic potentials of multi-element chemical systems. The potential energy surface of a multi-element system is represented as a many-body expansion of parametrized potentials which are functions of atom positions, atom types, and parameters. The proper orthogonal decomposition is employed to decompose the parametrized potentials as a linear combination of orthogonal basis functions. The orthogonal basis functions are used to construct proper orthogonal descriptors based on the elements of atoms, thus leading to multi-element descriptors. We compose the multi-element proper orthogonal descriptors to develop linear and quadratic interatomic potentials. We devise an algorithm to efficiently compute the total energy and forces of the interatomic potentials constructed from the proper orthogonal descriptors. The potentials are demonstrated for indium phosphide and titanium dioxide in comparison with the spectral neighbor analysis potential (SNAP) and atomic cluster expansion (ACE) potentials.

Keywords: interatomic potentials, machine learning potentials, proper orthogonal descriptors, atomic cluster expansion, spectral neighbor analysis potential

1. Introduction

Multi-element systems such as alloys, compounds, and composite materials are used in numerous applications and products. The properties of these classes of materials vary with both chemical structures and component compositions. *Ab initio* methods for self-consistent calculation of the

electronic structures provide the most accurate modeling technique to understanding physical and chemical properties of multi-element systems. As *ab initio* methods can be extremely expensive due to their high computational complexity, they are restricted to solving small-scale systems with thousands of atoms at most. Interatomic potentials represent the potential energy surface of a system as a function of atomic positions and types, leaving out the detailed electronic structures. As most interatomic potentials have a computational complexity that scales linearly with the number of atoms, they enable molecular dynamics simulations of large-scale systems with millions or even billions of atoms.

An interatomic potential is essentially a mathematical model that takes the full quantum many-body problem and casts it into computationally tractable expressions for the total energy as the sum of individual atom contributions. However, this simplification can be done in many different ways, giving rise to the numerous different types of interatomic potentials in the literature. The simplest and most efficient potentials are two-body potentials which express the energies and forces solely in terms of pairwise interactions between nearby atoms. Over the years, sophisticated empirical potentials have been developed to treat a wide variety of systems with different degrees of complexity. More often than not, existing empirical potentials are recalibrated by reparameterizing the existing set of parameters or extending the energy formula by adding terms and then parameterizing the entire potential anew. This results in many different forms and sets of parameters for widely-used empirical potentials such as EAM [1], Stillinger-Weber [2], Tersoff [3], EDIP [4], REBO [5], ReaxFF [6].

In recent years, a significant trend has emerged in the form of machine learning (ML) interatomic potentials, where the potential energy surface is described as a composition of local environment descriptors [7, 8, 9]. In order to obtain an accurate and efficient ML potential, the descriptors must meet several requirements. First and foremost, the descriptors must be invariant with respect to permutation, rotation, translation, and reflection of atoms in the system. Second, the descriptors need to be differentiable with respect to the atomic positions to enable the calculation of analytic gradients for the forces. Third, the descriptors must provide a detailed structural description of the local atomic environment to produce accurate and transferable potentials. Lastly, since the transformation from atom coordinates onto the descriptors has to be carried out for every atom, the computation of the descriptors has to be fast to produce efficient potentials. Examples of

ML potentials include the neural network potential (NNP) [10, 11, 12], the Gaussian approximation potential (GAP) [13, 14, 15], the spectral neighbor analysis potential (SNAP) [16, 17], moment tensor potentials (MTP) [18, 19], and the atomic cluster expansion (ACE) [20, 21, 9]. A recent work [22] assesses performance of SNAP, GAP, NNP, MTP potentials on a diverse dataset of bcc and fcc metals, as well as diamond group IV semiconductors.

In a recent work [23], we introduce a new method to represent atomic neighbourhood environments with the so-called proper orthogonal descriptors (PODs) inspired by the reduced basis method [24, 25, 26, 27, 28, 29] for parametrized partial differential equations. The POD potential is expressed as a linear combination of the proper orthogonal descriptors and fitted against density functional theory (DFT) data by using least-squares regression. The POD potential is demonstrated on single-element systems of Li, Mo, Cu, Ni, Si, Ge, Ta elements and found to provide as accurate predictions as both SNAP and ACE potentials. The POD potential is studied in the recent work [30] on the influence of model complexity on simulated properties and further extended in [31] to higher-order interactions. In [31], the POD potential is shown to admit the atom density formulation that allows for an efficient implementation of many-body POD descriptors.

In this paper, we extend our previous work [23] to develop proper orthogonal descriptors for multi-element chemical systems. The potential energy surface of a multi-element system is represented as a many-body expansion of parametrized potentials which are functions of atom positions, atom types, and parameters. The orthogonal basis functions are formed by applying the proper orthogonal decomposition to the parametrized potentials and transformed into proper orthogonal descriptors according to the chemical elements of atoms, thus leading to multi-element descriptors. Systems with more elements usually have more complex atomic environments than those with less elements. Hence, increasing the number of elements usually leads to an increase in the number of descriptors in order for the potential to provide accurate predictions for multi-element systems, which in turn results an increase in the computational cost. We emphasize that the multi-element proper orthogonal descriptors only need to scale the size of the model with actual chemical complexity and not with the combinatorial complexity of treating chemical species.

To deal with the chemical complexity of multi-element systems, we develop two different POD potentials by composing the descriptors in two different ways. The first POD potential is expressed as a linear combination

of the multi-element descriptors. For the second POD potential, we compose the original multi-element descriptors to construct quadratic descriptors that can capture higher-body interactions and provide more accurate predictions for multi-element systems. We develop an algorithm to evaluate the quadratic descriptors and their derivatives without increasing the overall computational cost. The second POD potential has the potential to effectively deal with chemical complexity of multi-element systems because (i) the cost of evaluating each of its descriptors is independent of the number of elements, (ii) it is able to generate linear models with sufficiently large number of descriptors, and (iii) it can retain the computational complexity of the first POD potential. Indeed, when the two POD potentials are demonstrated for indium phosphide and titanium dioxide, the second POD potential is found to be significantly more accurate than the first POD potential for the same computational cost. The performance improvement of the second POD potential over the first POD potential can be attributed to its capability of having considerably more descriptors to capture chemical complexity of multi-element systems.

The development of many-body descriptors for multi-element chemical systems have attracted considerable interest [32, 33, 16, 34, 35, 36, 37, 38, 39, 40, 41]. This interest stems from the wider range of applications and the needs for developing ML potentials that are efficient and accurate even though the atomic systems have a large number of elements. The complexity scaling with the number of elements can restrict the use of ML potentials in applications with many chemical elements, if the large size and computational cost of ML models increase rapidly with the number of elements. Various techniques to tackle this scaling problem have been proposed including element weighting [32, 33, 16], element embedding [34, 35], directly reducing the element-sensitive correlation order [36], low-rank tensor-train approximations for lattice models [37], tensor-reduced atomic density representations [38], and data-driven approach for selecting the most relevant subsets or compressing the original features [39, 40, 41].

In the element weighting approach [32, 33, 16], the number of model coefficients scales linearly with the number of elements and the computational complexity of evaluating the descriptors is independent of the number of elements. While this approach reduces the number of descriptors and the computational cost, it may also reduce the accuracy of the resulting potential compared to the original model. This observation is the main motivation behind the explicit multi-element extension of the element-weighted SNAP

potential [42]. In the element embedding approach [34, 35], the number of coefficients for the radial basis scales quadratically with the number of elements and the computational complexity of evaluating the descriptors is independent of the number of elements. However, this approach complicates the training process since it can lead to a nonlinear optimization problem for the model coefficients. Different element weighting and element embedding strategies for compressing local atomic neighbourhood descriptors are discussed in [36]. A tensor-reduced representation of the local atomic environment further reduces the size of the basis by taking element-wise products across the embedded channels rather than a full tensor product [38]. Although the number of descriptors does not depend on the number of chemical elements, the approach requires the specification of weight matrices for all the embedded channels. In our approach, multi-element descriptors are constructed from the combination of chemical elements without the use of element weighting or embedding.

The paper is organized as follows. We introduce multi-element proper orthogonal descriptors in Section 2 and develop the two POD potentials in Section 3. In Section 4, we describe an optimization procedure to fit POD potentials. In Section 5, we present numerical results to assess the performance of not only the POD potentials but also the ACE and SNAP potentials. Finally, in Section 6, we make a number of concluding remarks on the results as well as future work.

2. Multi-Element Proper Orthogonal Descriptors

2.1. Parametrized potential energy surface

We consider a multi-element system of N atoms with N_e unique elements. We denote by \mathbf{r}_n and Z_n position vector and type of an atom n in the system, respectively. Note that we have $Z_n \in \{1, \dots, N_e\}$, $\mathbf{R} = (\mathbf{r}_1, \mathbf{r}_2, \dots, \mathbf{r}_N) \in \mathbb{R}^{3N}$, and $\mathbf{Z} = (Z_1, Z_2, \dots, Z_N) \in \mathbb{N}^N$. The potential energy surface (PES) of the system can be expressed as a many-body expansion of the form

$$\begin{aligned}
 E(\mathbf{R}, \mathbf{Z}, \boldsymbol{\eta}, \boldsymbol{\mu}) &= \sum_i V^{(1)}(\mathbf{r}_i, Z_i, \boldsymbol{\eta}, \boldsymbol{\mu}^{(1)}) + \frac{1}{2} \sum_{i,j} V^{(2)}(\mathbf{r}_i, \mathbf{r}_j, Z_i, Z_j, \boldsymbol{\eta}, \boldsymbol{\mu}^{(2)}) \\
 &+ \frac{1}{6} \sum_{i,j,k} V^{(3)}(\mathbf{r}_i, \mathbf{r}_j, \mathbf{r}_k, Z_i, Z_j, Z_k, \boldsymbol{\eta}, \boldsymbol{\mu}^{(3)}) + \dots
 \end{aligned}
 \tag{1}$$

where $V^{(1)}$ is the one-body potential often used for representing external field or energy of isolated elements, and the higher-body potentials $V^{(2)}, V^{(3)}, \dots$ are symmetric and zero if two or more indices take identical values. The superscript on each potential denotes its body order. Each q -body potential $V^{(q)}$ depends on $\boldsymbol{\mu}^{(q)}$ which are sets of parameters to fit the PES. Note that $\boldsymbol{\mu}$ is a collection of all potential parameters $\boldsymbol{\mu}^{(1)}, \boldsymbol{\mu}^{(2)}, \boldsymbol{\mu}^{(3)}$, etc, and that $\boldsymbol{\eta}$ is a set of hyperparameters. Each potential $V^{(q)}$ depends on the same hyperparameters.

In the absence of external fields, the PES should not depend on the absolute position of atoms, but only on the relative positions. This means that the PES can be rewritten as a function of interatomic distances and angles between the bonds as

$$\begin{aligned}
 E(\mathbf{R}, \mathbf{Z}, \boldsymbol{\eta}, \boldsymbol{\mu}) = & \sum_i V^{(1)}(Z_i, \boldsymbol{\eta}, \boldsymbol{\mu}^{(1)}) + \frac{1}{2} \sum_{i,j} V^{(2)}(r_{ij}, Z_i, Z_j, \boldsymbol{\eta}, \boldsymbol{\mu}^{(2)}) \\
 & + \frac{1}{6} \sum_{i,j,k} V^{(3)}(r_{ij}, r_{ik}, \theta_{ijk}, Z_i, Z_j, Z_k, \boldsymbol{\eta}, \boldsymbol{\mu}^{(3)}) + \dots
 \end{aligned} \tag{2}$$

where each potential is a function of interatomic distances $r_{ij} = |\mathbf{r}_i - \mathbf{r}_j|$, bond angles θ_{ijk} , potential parameters, and the hyperparameters.

A wide variety of interatomic potentials such as Lennard-Jones potential, Morse potential, Stillinger-Weber potential, angle potentials, and dihedral potentials have the form (2). For these empirical potentials, however, both $\boldsymbol{\eta}$ and $\boldsymbol{\mu}$ are fixed to specific values. In other interatomic potentials such as EAM and Tersoff potentials, the many-body interactions are embedded into the terms of a pair potential in which the nature of the interaction is modified by the local environment of the atom via the bond order parameter, coordination number, or electron density.

Interatomic potentials rely on parameters to learn relationship between atomic environments and interactions. Since interatomic potentials are approximations by nature, their parameters need to be set to some reference values or fitted against experimental and/or numerical data by necessity. In simple potentials such as the Lennard-Jones and Morse potential, the parameters can be set to match the equilibrium bond length and bond strength of a dimer molecule or the surface energy of a solid. Many-body potentials often contain many parameters with limited interpretability and need to be optimized by fitting their parameters against a larger set of data. Typically, potential fitting finds optimal parameters, $\boldsymbol{\mu}^*$, to minimize a certain

loss function of the predicted quantities and data. Since the fitted potential depends on the data set used to fit it, different data sets will yield different optimal parameters and thus different fitted potentials. When fitting the same functional form on Q different data sets, we would obtain Q different optimized potentials, $E(\mathbf{R}, \mathbf{Z}, \boldsymbol{\eta}, \boldsymbol{\mu}_q^*)$, $1 \leq q \leq Q$. These optimized potentials are typically intended to predict properties that are similar to those they are fitted to. Inaccurate predictions may occur when they are used to predict out-of-fitting properties. Consequently, there exist many different sets of optimized parameters for widely-used empirical potentials such as EAM [1], Stillinger-Weber [2], Tersoff [3], EDIP [4], REBO [5], ReaxFF [6].

Following the philosophy of the reduced basis method [24, 25, 26, 27, 28, 29] for parametrized partial differential equations, the parametrized PES can be viewed as a parametric manifold of potential energies

$$\mathcal{M} = \{E(\mathbf{R}, \mathbf{Z}, \boldsymbol{\eta}, \boldsymbol{\mu}) \mid \boldsymbol{\mu} \in \Omega^\mu\} \quad (3)$$

where Ω^μ is a parameter domain in which $\boldsymbol{\mu}$ resides. The parametric manifold \mathcal{M} contains potential energy surfaces for all values of $\boldsymbol{\mu} \in \Omega^\mu$. Therefore, the parametric manifold yields a much richer and more transferable atomic representation than any particular individual PES $E(\mathbf{R}, \mathbf{Z}, \boldsymbol{\eta}, \boldsymbol{\mu}^*)$. In what follows, we propose specific forms of the parametrized potentials for two-body and three-body interactions, and construct corresponding descriptors by using the proper orthogonal decomposition.

2.2. Two-body proper orthogonal descriptors

We adopt the usual assumption that the direct interaction between two atoms vanishes smoothly when their distance is greater than the outer cutoff distance r_{\max} . Furthermore, we assume that two atoms can not get closer than the inner cutoff distance r_{\min} due to the Pauli repulsion principle. The two-body descriptors are constructed upon a set of orthogonal basis functions, $U_i^{(2)}(r, \boldsymbol{\eta})$, $1 \leq i \leq N_b^{(2)}$, which are defined in the domain $r \in [r_{\min}, r_{\max}]$ such that

$$\int_{r_{\min}}^{r_{\max}} U_i^{(2)}(r, \boldsymbol{\eta}) U_j^{(2)}(r, \boldsymbol{\eta}) dr = \delta_{ij}, \quad i, j = 1, \dots, N_b^{(2)}. \quad (4)$$

Here $N_b^{(2)}$ is the number of basis functions for the two-body interaction. In [9], a general procedure was proposed to construct radial basis functions

which are orthogonal with respect to a user-defined inner product. In particular, the orthogonal basis functions are constructed from a set of orthogonal polynomials on $[a, b]$, a coordinate transformation $\xi : [r_{\min}, r_{\max}] \rightarrow [a, b]$, a density function $\rho(r)$, and a cut-off function $f_{\text{cut}}(r)$. The procedure allows for a wide range of potential optimization of the radial basis by optimizing the coordinate transformation and the density function. Appropriate choices of the coordinate transformation and the density function have been proposed in [9]. Our method differs from the approach introduced in [9] as follows. Instead of using orthogonal polynomials to construct the radial basis, we will use two families of parametrized radial functions. Our method is also related to the principal component analysis [40] that generates optimal radial basis in terms of its ability to linearly compress the information encoded in the variance of the density coefficients. The optimal radial basis can be determined as a contraction of any complete primitive basis, and evaluated efficiently by approximating it with splines. In [40], the Gaussian type orbital (GTO) basis and the discrete variable representation (DVR) basis are used as complete primitive basis to construct the optimal radial basis.

We describe a method to systematically construct orthogonal basis functions from families of parametrized functions. We introduce two families of parametrized radial functions

$$\phi(r, r_{\min}, r_{\max}, \alpha, \beta) = \frac{\sin(\alpha\pi x)}{r - r_{\min}}, \quad \varphi(r, \gamma) = \frac{1}{r^\gamma}, \quad (5)$$

where the scaled distance function x is defined below to enrich the two-body manifold

$$x(r, r_{\min}, r_{\max}, \beta) = \frac{e^{-\beta(r-r_{\min})/(r_{\max}-r_{\min})} - 1}{e^{-\beta} - 1}. \quad (6)$$

We introduce the following function as a convex combination of the two functions in (5)

$$\psi(r, r_{\min}, r_{\max}, \alpha, \beta, \gamma, \kappa) = \kappa\phi(r, r_{\min}, r_{\max}, \alpha, \beta) + (1 - \kappa)\varphi(r, \gamma). \quad (7)$$

The function ϕ in (5) is related to the zeroth spherical Bessel function, while the function φ is inspired by the n-m Lennard-Jones potential. Indeed, the 12-6 Lennard-Jones potential $V_{\text{LJ}}(r) = \frac{A}{r^{12}} - \frac{B}{r^6}$ can be expressed as $V_{\text{LJ}}(r) = A\varphi(r, 12) - B\varphi(r, 6)$. As a result, $V(r) = \sum_{\gamma=1}^{N_\gamma} A_k\varphi(r, \gamma)$ can describe both repulsive and attractive interactions between two atoms for any given large enough N_γ . Although the parameter γ can be real number, we choose a set

of consecutive positive integers $\{1, 2, \dots, N_\gamma\}$ to compute instances of the parametrized function φ by making use of the relation $\varphi(r, \gamma+1) = \varphi(r, \gamma)/r$. Similarly, we choose a set of consecutive integers $\{1, 2, \dots, N_\alpha\}$ for α to generate instances of the parametrized function ϕ because it allows us to use the formula $\sin((\alpha+1)\pi x) = \sin(\pi x)U_\alpha(\cos(\pi x))$ to compute these instances efficiently, where U_α are Chebyshev polynomials of the second kind. We take N_β values for the parameter β such that $\beta_k = (k-1)\beta_{\max}/(P_\beta - 1)$ for $k = 1, 2, \dots, N_\beta$, where $\beta_{\max} = 4.0$. Hence, the total number of parameter points is $N_s = N_\alpha N_\beta + N_\gamma$. Although $N_\alpha, N_\beta, N_\gamma$ can be chosen conservatively large, we find that $N_\alpha = 6, N_\beta = 3, N_\gamma = 12$ (namely, $N_s = 30$) are adequate to enabling the function ψ to characterize a diverse spectrum of two-body interactions within the cut-off interval (r_{\min}, r_{\max}) .

Our method allows for the addition of other families of parametrized functions (e.g., the Morse potential) to define ψ in (7). More broadly, the method allows for a systematic combination of empirical potentials to define orthogonal descriptors based on the following parametrized potential

$$W^{(2)}(r_{ij}, \boldsymbol{\eta}, \boldsymbol{\mu}^{(2)}) = f_c(r_{ij}, \boldsymbol{\eta})\psi(r_{ij}, \boldsymbol{\eta}, \boldsymbol{\mu}^{(2)}) \quad (8)$$

where $\boldsymbol{\eta}$ includes the inner and outer cut-off radii, $\boldsymbol{\mu}^{(2)}$ consists of the remaining parameters, and f_c is a cut-off function. In this paper, we use the following cut-off function

$$f_c(r_{ij}, r_{\min}, r_{\max}) = \exp\left(1 - \frac{1}{\sqrt{\left(1 - \frac{(r-r_{\min})^3}{(r_{\max}-r_{\min})^3}\right)^2 + 10^{-6}}}\right), \quad (9)$$

which ensures the smooth vanishing of the potential and its derivative beyond r_{\max} . Other cut-off functions can also be used. Given N_s parameter tuples $\boldsymbol{\mu}_\ell^{(2)}, 1 \leq \ell \leq N_s$, we introduce the following set of snapshots

$$\xi_\ell(r_{ij}, \boldsymbol{\eta}) = W^{(2)}(r_{ij}, \boldsymbol{\eta}, \boldsymbol{\mu}_\ell^{(2)}), \quad \ell = 1, \dots, N_s. \quad (10)$$

We employ the proper orthogonal decomposition [43, 44, 45] to generate an orthogonal basis set as follows

$$U_m^{(2)}(r_{ij}, \boldsymbol{\eta}) = \sum_{\ell=1}^{N_s} A_{\ell m}(\boldsymbol{\eta}) \xi_\ell(r_{ij}, \boldsymbol{\eta}), \quad m = 1, \dots, N_b^{(2)}, \quad (11)$$

where the matrix $\mathbf{A} \in \mathbb{R}^{N_s \times N_s}$ consists of eigenvectors of the eigenvalue problem

$$\mathbf{C}\mathbf{a} = \lambda\mathbf{a}, \quad (12)$$

with

$$C_{ij} = \frac{1}{N_s} \int_{r_{\min}}^{r_{\max}} \xi_i(x, \boldsymbol{\eta}) \xi_j(x, \boldsymbol{\eta}) dx, \quad 1 \leq i, j \leq N_s.$$

Note that the eigenvalues $\lambda_\ell, 1 \leq \ell \leq N_s$, are ordered such that $\lambda_1 \geq \lambda_2 \geq \dots \geq \lambda_{N_s}$, and that the matrix \mathbf{A} is pre-computed and stored. Owing to the rapid convergence of the proper orthogonal decomposition, a small number of orthogonal basis functions is needed to obtain accurate approximation.

Finally, the two-body proper orthogonal descriptors at each atom i are computed by summing the orthogonal basis functions over the neighbors of atom i and numerating on the atom types as follows

$$D_{iml(p,q)}^{(2)}(\boldsymbol{\eta}) = \begin{cases} \sum_{\{j|Z_j=q\}} U_m^{(2)}(r_{ij}, \boldsymbol{\eta}), & \text{if } Z_i = p \\ 0, & \text{if } Z_i \neq p \end{cases} \quad (13)$$

for $1 \leq i \leq N, 1 \leq m \leq N_b^{(2)}, 1 \leq q, p \leq N_e$. Here $l(p, q)$ is a symmetric index mapping such that

$$l(p, q) = \begin{cases} q + (p-1)N_e - p(p-1)/2, & \text{if } q \geq p \\ p + (q-1)N_e - q(q-1)/2, & \text{if } q < p. \end{cases} \quad (14)$$

The number of descriptors per atom is thus $N_b^{(2)} N_e (N_e + 1) / 2$. It is important to note that the orthogonal basis functions defined in (11) do not depend on the atomic numbers Z_i and Z_j . Therefore, the cost of evaluating the basis functions and their derivatives with respect to r_{ij} is independent of the number of elements N_e .

2.3. Three-body proper orthogonal descriptors

In order to provide proper orthogonal descriptors for three-body interactions, we introduce a three-body parametrized potential as follows

$$W^{(3)}(r_{ij}, r_{ik}, \theta_{ijk}, \boldsymbol{\eta}, \boldsymbol{\mu}^{(3)}) = \psi(r_{ij}, r_{\min}, r_{\max}, \alpha, \beta, \gamma, \kappa) f_c(r_{ij}, r_{\min}, r_{\max}) \\ \psi(r_{ik}, r_{\min}, r_{\max}, \alpha, \beta, \gamma, \kappa) f_c(r_{ik}, r_{\min}, r_{\max}) \\ \cos(\sigma\theta_{ijk} + \zeta) \quad (15)$$

where σ is the periodic multiplicity, ζ is the equilibrium angle, $\boldsymbol{\mu}^{(3)} = (\alpha, \beta, \gamma, \kappa, \sigma, \zeta)$. The potential (15) provides an angular fingerprint of the atomic environment through the bond angles θ_{ijk} formed with each pair of neighbors j and k . Compared to the two-body potential (8), the three-body potential (15) has two extra parameters (σ, ζ) associated with the angular component. Ideally, ζ is the physical equilibrium angle of the molecular system. However, since the function $\cos(\sigma\theta + \zeta)$ can be approximated well by a linear combination of Chebyshev polynomials of the first kind, $T_{n-1}(\cos\theta) = \cos((n-1)\theta)$, $n = 1, \dots, N_a$, for large enough N_a , we take ζ to be zero and choose σ as non-negative integers. Hence, the angular basis functions are given by

$$U_n^a(\theta_{ijk}) = \cos((n-1)\theta_{ijk}), \quad n = 1, \dots, N_a, \quad (16)$$

where N_a is the number of angular basis functions. The orthogonal basis functions for the parametrized potential (15) are computed as follows

$$U_{mn}^{(3)}(r_{ij}, r_{ik}, \theta_{ijk}, \boldsymbol{\eta}) = U_m^{(2)}(r_{ij}, \boldsymbol{\eta}) U_n^{(2)}(r_{ik}, \boldsymbol{\eta}) U_n^a(\theta_{ijk}), \quad (17)$$

for $1 \leq m \leq N_r, 1 \leq n \leq N_a$, where $U_m^{(2)}(r_{ij}, \boldsymbol{\eta})$ are the two-body orthogonal basis functions. The number of three-body orthogonal basis functions is equal to $N_b^{(3)} = N_r N_a$.

Finally, the three-body proper orthogonal descriptors at each atom i are obtained by summing (17) over the neighbors j and k of atom i as

$$D_{imn\ell(p,q,s)}^{(3)}(\boldsymbol{\eta}) = \begin{cases} \sum_{\{j|Z_j=q\}} \sum_{\{k|Z_k=s\}} U_{mn}^{(3)}(r_{ij}, r_{ik}, \theta_{ijk}, \boldsymbol{\eta}), & \text{if } Z_i = p \\ 0, & \text{if } Z_i \neq p \end{cases} \quad (18)$$

for $1 \leq i \leq N, 1 \leq m \leq N_r, 1 \leq n \leq N_a, 1 \leq q, p, s \leq N_e$, where

$$\ell(p, q, s) = \begin{cases} s + (q-1)N_e - q(q-1)/2 + (p-1)N_e(1+N_e)/2, & \text{if } s \geq q \\ q + (s-1)N_e - s(s-1)/2 + (p-1)N_e(1+N_e)/2, & \text{if } s < q. \end{cases} \quad (19)$$

The number of three-body descriptors per atom is thus $N_b^{(3)} N_e^2 (N_e + 1)/2$. It remains to describe the computational complexity of the proper orthogonal descriptors.

2.4. Computational complexity of proper orthogonal descriptors

We analyze the computational complexity of evaluating the descriptors and their derivatives with respect to r_{ij} . It follows from (11) that

$$\frac{\partial U_m^{(2)}(r_{ij}, \boldsymbol{\eta})}{\partial r_{ij}} = \sum_{\ell=1}^{N_s} A_{\ell m}(\boldsymbol{\eta}) \frac{\partial \xi_{\ell}(r_{ij}, \boldsymbol{\eta})}{\partial r_{ij}}, \quad m = 1, \dots, N_b^{(2)}. \quad (20)$$

and from (17) that

$$\begin{aligned} \frac{\partial U_{mn}^{(3)}(r_{ij}, r_{ik}, \theta_{ijk}, \boldsymbol{\eta})}{\partial r_{ij}} &= \frac{\partial U_m^{(2)}(r_{ij}, \boldsymbol{\eta})}{\partial r_{ij}} U_m^{(2)}(r_{ik}, \boldsymbol{\eta}) \cos((n-1)\theta_{ijk}) \\ \frac{\partial U_{mn}^{(3)}(r_{ij}, r_{ik}, \theta_{ijk}, \boldsymbol{\eta})}{\partial r_{ik}} &= U_m^{(2)}(r_{ij}, \boldsymbol{\eta}) \frac{\partial U_m^{(2)}(r_{ik}, \boldsymbol{\eta})}{\partial r_{ik}} \cos((n-1)\theta_{ijk}), \\ \frac{\partial U_{mn}^{(3)}(r_{ij}, r_{ik}, \theta_{ijk}, \boldsymbol{\eta})}{\partial \theta_{ijk}} &= -(n-1) U_m^{(2)}(r_{ij}, \boldsymbol{\eta}) U_m^{(2)}(r_{ik}, \boldsymbol{\eta}) \sin((n-1)\theta_{ijk}). \end{aligned} \quad (21)$$

We assume that each atom has the same number of neighbors N_n . The total number of neighbors is thus NN_n for all atoms. The operation count for computing the orthogonal basis functions in (11) and their derivatives in (20) is thus $O(NN_n N_s N_b^{(2)})$. The operation count for evaluating the two-body PODs in (13) and their derivatives is $O(NN_n N_b^{(2)})$. The operation count for computing the three-body orthogonal basis functions in (17) and their derivatives in (21) is $O(NN_n^2 N_b^{(3)})$. Therefore, the computational complexity of the three-body PODs (18) and their derivatives is also $O(NN_n^2 N_b^{(3)})$. Since the three-body PODs are more expensive than the two-body PODs, the overall computational complexity is $O(NN_n^2 N_b^{(3)})$.

Of course, systems with more elements often have more complex atomic environments than those with less elements. Hence, increasing the number of elements may require an increase in the number of descriptors, thereby increasing the computational cost of a potential constructed from these descriptors. To deal with the chemical complexity of multi-element systems, we introduce a quadratic POD potential by composing the multi-element descriptors to construct quadratic descriptors that can capture higher-body interactions and chemical complexity of multi-element systems. We develop an algorithm to evaluate the quadratic descriptors and their derivatives without increasing the overall computational cost. The quadratic POD potential

has the following features: (i) the cost of evaluating each of its descriptors is independent of the number of elements, (ii) it can generate linear models with large number of descriptors, and (iii) it can retain the computational complexity of the linear POD potential. The next section describes the construction of the linear and quadratic POD potentials.

3. Proper Orthogonal Descriptor Potentials

3.1. The linear POD potential

We use the proper orthogonal descriptors to define the atomic energies

$$E_i^L(\boldsymbol{\eta}) = \sum_{p=1}^{N_e} c_p^{(1)} D_{ip}^{(1)} + \sum_{m=1}^{N_b^{(2)}} \sum_{l=1}^{N_e(N_e+1)/2} c_{ml}^{(2)} D_{iml}^{(2)}(\boldsymbol{\eta}) + \sum_{m=1}^{N_r} \sum_{n=1}^{N_a} \sum_{\ell=1}^{N_e^2(N_e+1)/2} c_{mnl}^{(3)} D_{imnl}^{(3)}(\boldsymbol{\eta}), \quad 1 \leq i \leq N, \quad (22)$$

where $D_{ip}^{(1)}, D_{iml}^{(2)}, D_{imnl}^{(3)}$ are the one-body, two-body descriptors, respectively, and $c_p^{(1)}, c_{ml}^{(2)}, c_{mnl}^{(3)}$ are their respective expansion coefficients. In a more compact notation that implies summation over descriptor indices, the atomic energies can be written as

$$E_i^L(\boldsymbol{\eta}) = \sum_{p=1}^{N_e} c_p^{(1)} D_{ip}^{(1)} + \sum_{k=1}^{N_d^{(2)}} c_k^{(2)} D_{ik}^{(2)} + \sum_{m=1}^{N_d^{(3)}} c_m^{(3)} D_{im}^{(3)} \quad (23)$$

where $N_d^{(2)} = N_b^{(2)} N_e(N_e+1)/2$ and $N_d^{(3)} = N_b^{(3)} N_e^2(N_e+1)/2$ are the number of two-body and three-body descriptors, respectively. The one-body descriptors are defined as follows

$$D_{ip}^{(1)} = \begin{cases} 1, & \text{if } Z_i = p \\ 0, & \text{if } Z_i \neq p \end{cases} \quad (24)$$

for $1 \leq i \leq N, 1 \leq p \leq N_e$. The one-body descriptors are independent of atom positions, but dependent on atom types.

In actual implementation, we calculate the potential energy and atomic forces without computing and storing the descriptors. We note from (13),

(18), and (22) that the atomic energies can be expressed in terms of the orthogonal basis functions as

$$E_i^L(\boldsymbol{\eta}) = c_{Z_i}^{(1)} + \sum_j \sum_{m=1}^{N_b^{(2)}} c_{ml(Z_i, Z_j)}^{(2)} U_m^{(2)}(r_{ij}, \boldsymbol{\eta}) + \sum_j \sum_k \sum_{m=1}^{N_r} \sum_{n=1}^{N_a} c_{mnl(Z_i, Z_j, Z_k)}^{(3)} U_{mn}^{(3)}(r_{ij}, r_{ik}, \theta_{ijk}, \boldsymbol{\eta}), \quad (25)$$

where $l(Z_i, Z_j)$ and $l(Z_i, Z_j, Z_k)$ are the index mappings defined in (14) and (19), respectively. In order to calculate the atomic forces, we need to compute the derivatives of the atomic energies $E_i^L(\boldsymbol{\eta})$ with respect to r_{ij} , r_{ik} , and θ_{ijk} . This requires us to compute the derivatives of the orthogonal basis functions in (20) and (21) with $O(NN_n^2N_b^{(3)})$ as discussed in the previous section. Hence, the overall computational cost of the linear POD potential is $O(NN_n^2N_b^{(3)})$. The cost is linear in the number of atoms and the number of three-body basis functions, but quadratic in the number of neighbors.

The potential energy surface is then obtained by summing atomic energies E_i^L for all atoms i in the system as follows

$$E^L = \sum_{p=1}^{N_e} c_p^{(1)} d_p^{(1)} + \sum_{k=1}^{N_d^{(2)}} c_k^{(2)} d_k^{(2)} + \sum_{m=1}^{N_d^{(3)}} c_m^{(3)} d_m^{(3)}, \quad (26)$$

where

$$d_p^{(1)} = \sum_{i=1}^N D_{ip}^{(1)}, \quad d_k^{(2)} = \sum_{i=1}^N D_{ik}^{(2)}, \quad d_m^{(3)} = \sum_{i=1}^N D_{im}^{(3)}, \quad (27)$$

are one-body, two-body, and three-body global descriptors, respectively. The atomic forces are thus given by

$$\mathbf{F}^L = - \sum_{k=1}^{N_d^{(2)}} c_k^{(2)} \nabla d_k^{(2)} - \sum_{m=1}^{N_d^{(3)}} c_m^{(3)} \nabla d_m^{(3)} \quad (28)$$

where the symbol ∇ denotes the derivatives of the global descriptors with respect to atom positions.

3.2. The quadratic POD potential

To construct a quadratic POD potential, we introduce a set of quadratic per-atom descriptors

$$D_{ikm}^{(2*3)}(\mathbf{R}, \mathbf{Z}, \boldsymbol{\eta}) = \frac{1}{2N} \left(D_{ik}^{(2)} d_m^{(3)} + D_{im}^{(3)} d_k^{(2)} \right) \quad (29)$$

for $1 \leq i \leq N, 1 \leq k \leq N_d^{(2)}, 1 \leq m \leq N_d^{(3)}$, where $d_k^{(2)}$ and $d_m^{(3)}$ are two-body and three-body global descriptors defined in (27). Because the quadratic per-atom descriptors are defined in terms of the products of the local descriptors and the global descriptors, they depend on positions and chemical identities of all atoms in the system. Therefore, the quadratic per-atom descriptors encapsulate the global environments of the atomic configuration. The per-atom energies of the quadratic POD potential are defined as

$$E_i^{\text{Q}}(\mathbf{R}, \mathbf{Z}, \boldsymbol{\eta}) = E_i^{\text{L}} + \sum_{k=1}^{N_d^{(2)}} \sum_{m=1}^{N_d^{(3)}} c_{km}^{(2*3)} D_{ikm}^{(2*3)}(\mathbf{R}, \mathbf{Z}, \boldsymbol{\eta}) \quad (30)$$

where E_i^{L} defined in (23) are the per-atom energies of the linear POD potential and $c_{km}^{(2*3)}$ are coefficients associated with the quadratic per-atom descriptors. While E_i^{L} depend on positions and chemical identities of atoms within the cut-off distance r_{max} from the central atom i , E_i^{Q} depend on positions and chemical identities of all atoms in the system due to the quadratic per-atom descriptors.

The PES of the quadratic POD potential is obtained by summing atomic energies E_i^{Q} for all atoms i in the system as follows

$$E^{\text{Q}} = \sum_{p=1}^{N_e} c_p^{(1)} d_p^{(1)} + \sum_{k=1}^{N_d^{(2)}} c_k^{(2)} d_k^{(2)} + \sum_{m=1}^{N_d^{(3)}} c_m^{(3)} d_m^{(3)} + \sum_{k=1}^{N_d^{(2)}} \sum_{m=1}^{N_d^{(3)}} c_{km}^{(2*3)} d_{km}^{(2*3)}, \quad (31)$$

where the quadratic global descriptors are calculated as

$$d_{km}^{(2*3)} = \sum_{i=1}^N D_{ikm}^{(2*3)} = \frac{1}{N} \left(\sum_{i=1}^N D_{ik}^{(2)} \right) \left(\sum_{i=1}^N D_{im}^{(3)} \right) = \frac{1}{N} d_k^{(2)} d_m^{(3)}, \quad (32)$$

for $1 \leq k \leq N_d^{(2)}, 1 \leq m \leq N_d^{(3)}$. The atomic forces are calculated as

$$\mathbf{F}^{\text{Q}} = - \sum_{k=1}^{N_d^{(2)}} c_k^{(2)} \nabla d_k^{(2)} - \sum_{m=1}^{N_d^{(3)}} c_m^{(3)} \nabla d_m^{(3)} - \sum_{k=1}^{N_d^{(2)}} \sum_{m=1}^{N_d^{(3)}} c_{km}^{(2*3)} \nabla d_{km}^{(2*3)}. \quad (33)$$

Hence, the quadratic POD potential is the linear POD potential augmented with the additional terms due to the quadratic global descriptors .

In order to efficiently evaluate the quadratic POD potential, we rewrite its PES as

$$E^{\text{Q}} = \sum_{p=1}^{N_e} c_p^{(1)} d_p^{(1)} + \sum_{k=1}^{N_d^{(2)}} \left(c_k^{(2)} + 0.5b_k^{(2)} \right) d_k^{(2)} + \sum_{m=1}^{N_d^{(3)}} \left(c_m^{(3)} + 0.5b_m^{(3)} \right) d_m^{(3)}, \quad (34)$$

and the atomic forces as

$$\mathbf{F}^{\text{Q}} = - \sum_{k=1}^{N_d^{(2)}} \left(c_k^{(2)} + b_k^{(2)} \right) \nabla d_k^{(2)} - \sum_{m=1}^{N_d^{(3)}} \left(c_m^{(3)} + b_m^{(3)} \right) \nabla d_m^{(3)}, \quad (35)$$

where

$$b_k^{(2)} = \frac{1}{N} \sum_{m=1}^{N_d^{(3)}} c_{km}^{(2*3)} d_m^{(3)}, \quad k = 1, \dots, N_d^{(2)},$$

$$b_m^{(3)} = \frac{1}{N} \sum_{k=1}^{N_d^{(2)}} c_{km}^{(2*3)} d_k^{(2)}, \quad m = 1, \dots, N_d^{(3)}.$$
(36)

To calculate $b_k^{(2)}$ and $b_m^{(3)}$, we must compute the two-body and three-body global descriptors

$$d_{ml(p,q)}^{(2)}(\boldsymbol{\eta}) = \sum_{\{i|Z_i=p\}} \sum_{\{j|Z_j=q\}} U_m^{(2)}(r_{ij}, \boldsymbol{\eta})$$

$$d_{mnl(p,q,s)}^{(3)}(\boldsymbol{\eta}) = \sum_{\{i|Z_i=p\}} \sum_{\{j|Z_j=q\}} \sum_{\{k|Z_k=s\}} U_{mn}^{(3)}(r_{ij}, r_{ik}, \theta_{ijk}, \boldsymbol{\eta}),$$
(37)

with an operation count of $O(NN_n^2N_b^{(3)})$. The additional cost of calculating $b_k^{(2)}$ and $b_m^{(3)}$ in (36) is $O(N_d^{(2)}N_d^{(3)})$. Therefore, the computational cost of the quadratic POD potential is $O(NN_n^2N_b^{(3)} + N_d^{(2)}N_d^{(3)})$. If $N_d^{(2)}N_d^{(3)}$ is less than $NN_n^2N_b^{(3)}$, the computational complexity of the quadratic POD potential reduces to $O(NN_n^2N_b^{(3)})$, which is exactly the computational cost of the linear POD potential. This should be the case for most practical applications involving molecular dynamics simulations of large number of atoms.

The quadratic potential, with its comprehensive set of descriptors and incorporation of higher body orders, has the potential for more precise predictions than the linear potential. It achieves this without a significant increase in computational expense for many relevant systems, maintaining the same cost profile as its linear counterpart. Furthermore, it is possible for the quadratic potential to capture long-range interactions because its per-atom energies depend on all atoms in the system. In other words, the changes in the position of one atom affect the forces upon all atoms in the system. However, the quadratic descriptors do not inherit the notion of orthogonality from the two-body and three-body descriptors, and are incomplete in the sense that they do not span the systematic set of four-body descriptors. Nonetheless, this approach can be augmented for higher-order interactions through the integration of three-body descriptors with themselves, potentially expanding the predictive power of the model.

3.3. Connection with the quadratic SNAP potential

The quadratic POD potential bears similarities with the quadratic SNAP potential [17]. The main idea of the quadratic SNAP is to make new per-atom descriptors from the original per-atom descriptors as follows

$$D_{ikm}^{(2*3)} = D_{ik}^{(2)} D_{im}^{(3)}, \quad k = 1, \dots, N_d^{(2)}, m = 1, \dots, N_d^{(3)}. \quad (38)$$

The SNAP descriptors and our quadratic per-atom descriptors (29) are distinct in their dependency on atomic arrangements. Specifically, SNAP descriptors are influenced by the local environment surrounding a central atom i focusing on immediate atomic neighbors. In contrast, our quadratic per-atom descriptors consider interactions involving all atoms within the system and thus provide a more global description of atomic interactions. The SNAP global descriptors are calculated as

$$d_{km}^{(2*3)} = \sum_{i=1}^N D_{ikm}^{(2*3)} = \sum_{i=1}^N D_{ik}^{(2)} D_{im}^{(3)}. \quad (39)$$

We see that the quadratic global descriptors of the quadratic SNAP potential are not defined as the products of the original global descriptors, whereas those of the quadratic POD potential are as shown by (32). As a result, the quadratic SNAP potential cannot be written as a linear combination of the original global descriptors, whereas the quadratic POD potential can be as

shown by (34). The quadratic SNAP potential is slightly more expensive than the linear SNAP potential because evaluating the quadratic descriptors and their derivatives incurs an increase in computational cost and memory storage.

4. Potential Fitting

4.1. Weighted least-squares regression

Let J be the number of training configurations, with N_j being the number of atoms in the j th configuration. Let $\{E_j^*\}_{j=1}^J$ and $\{\mathbf{F}_j^*\}_{j=1}^J$ be the DFT energies and forces for J configurations. Next, we calculate the global descriptors and their derivatives for all training configurations. Let d_{jm} , $1 \leq m \leq M$, be the global descriptors associated with the j th configuration, where M is the number of global descriptors. We then form a matrix $\mathbf{A} \in \mathbb{R}^{J \times M}$ with entries $A_{jm} = d_{jm}/N_j$ for $j = 1, \dots, J$ and $m = 1, \dots, M$. Moreover, we form a matrix $\mathbf{B} \in \mathbb{R}^{\mathcal{N} \times M}$ by stacking the derivatives of the global descriptors for all training configurations from top to bottom, where $\mathcal{N} = 3 \sum_{j=1}^J N_j$. The coefficient vector \mathbf{c} of the linear expansion (23) is found by solving the following least-squares problem

$$\min_{\mathbf{c} \in \mathbb{R}^M} \beta \|\mathbf{A}(\boldsymbol{\eta})\mathbf{c} - \bar{\mathbf{E}}^*\|^2 + \|\mathbf{B}(\boldsymbol{\eta})\mathbf{c} + \mathbf{F}^*\|^2, \quad (40)$$

where β is a scalar to weight the energy contribution. Here $\bar{\mathbf{E}}^* \in \mathbb{R}^J$ is a vector of with entries $\bar{E}_j^* = E_j^*/N_j$ and \mathbf{F}^* is a vector of \mathcal{N} entries obtained by stacking $\{\mathbf{F}_j^*\}_{j=1}^J$ from top to bottom.

The training procedure is the same for both the linear and quadratic POD potentials. However, the quadratic POD potential is more expensive to train because the fitting of the quadratic POD potential still requires us to calculate and store the quadratic global descriptors and their gradient. Furthermore, the quadratic POD potential may require more training data in order to prevent over-fitting. In order to reduce the cost of fitting the second POD potential and avoid over-fitting, we can use subsets of two-body and three-body PODs for constructing the new descriptors.

4.2. Optimization of hyperparameters

The hyperparameters contain inner and outer cut-off distances for two-body and three-body interactions. They can affect the prediction performance of the resulting potential. We observe through our numerical experiences that longer cut-off distances do not necessarily translate to better

performance. Furthermore, setting them to some heuristic values may lead to an interatomic potential that can be less accurate than the potential obtained by optimizing the cut-off distances. Thus, we solve the following constrained optimization problem

$$\begin{aligned} & \min_{\boldsymbol{\eta} \in \Omega^n, \mathbf{c} \in \mathbb{R}^M} w \|\mathbf{A}(\boldsymbol{\eta})\mathbf{c}(\boldsymbol{\eta}) - \bar{\mathbf{E}}^*\|_{\text{MAE}} + (1-w) \|\mathbf{B}(\boldsymbol{\eta})\mathbf{c}(\boldsymbol{\eta}) - \mathbf{F}^*\|_{\text{MAE}} \\ & \text{subject to } (\beta^2 \mathbf{A}^T \mathbf{A} + \mathbf{B}^T \mathbf{B})\mathbf{c} = (\beta^2 \mathbf{A}^T \bar{\mathbf{E}}^* + \mathbf{B}^T \mathbf{F}^*) \end{aligned} \quad (41)$$

where $w \in [0, 1]$ is a given scalar weight, and $\|\cdot\|_{\text{MAE}}$ is defined as

$$\|\mathbf{e}\|_{\text{MAE}} = \frac{1}{n} \sum |e_i|. \quad (42)$$

Note that Ω^n is a domain in which the hyperparameters reside. The equality constraint in (41) is obtained from the optimality condition of the least-squares problem (40).

The optimization problem (41) is generally nonlinear and non-convex. Instead of directly solving the problem (41), we solve a surrogate problem by approximating the loss function in (41) using polynomial tensor-product interpolation. We select Q grid points $\{\boldsymbol{\eta}_q \in \Omega^n\}_{q=1}^Q$ and compute the loss function at those grid points. We then fit the loss values at the grid points to a tensor-product multivariate polynomial of certain degree to construct a surrogate model of the loss function. Finally, the gradient descent algorithm is used to minimize the surrogate model to obtain the hyperparameters. In order to be able to reach the global minimum, we start our gradient descent algorithm with a number of initial guesses randomly sampled in Ω^n .

5. Numerical Experiments

In this section, we assess the performance of POD potentials for indium phosphide and titanium dioxide. The linear POD potential in Section 3.1 and the quadratic POD potential in Section 3.2 shall be referred to as POD-I and POD-II, respectively. In addition, we present results with the ACE potential [9] and the explicit multi-element SNAP potential [42].

5.1. Indium phosphide

In [42], Cusentino et. al introduced an explicit multi-element SNAP potential and demonstrated it for indium phosphide (InP) dataset generated

using the Vienna Ab Initio Simulation Package (VASP). The InP dataset contains not only chemically unique environment but also high-energy defects which are intended to study radiation damage effects where collision cascades of sufficiently high energy leave behind high formation energy point defects. In addition to defect configurations, the dataset includes configurations for uniform expansion and compression (Equation of State), random cell shape modifications (Shear group), and uniaxially strained (Strain group) unit cells for zincblende crystal structure. In total, the dataset has 1894 configurations with atom counts per configuration ranging from 8 to 216. The InP data set is split into a training set (80%) and test set (20%) in order to assess the performance of POD potentials.

Table 1 provides the cutoff distances and the number of descriptors for POD-I, POD-II, and EME-SNAP, while Table 2 reports the polynomial degrees for ACE.¹ The number of descriptors for EME-SNAP is $N_d = N_e^4(J + 1)(J + 2)(J + 3/2)/3$. The number of descriptors for ACE depends on the body orders, the radial and angular degrees for each body order. For POD potentials, the optimization problem (41) is solved with $\beta = 100$ and $w = 0.8$. Figure 1 show the polynomial interpolation surrogate of the loss function for POD-I at $N_d = 170$. The surrogate loss function is smooth with multiple local minima. We see that cutoff distances affect the value of the loss function and thus the accuracy of the resulting potential. Therefore, it is beneficial to optimize these hyperparameters.

Table 3 provides mean absolute errors (MAEs) in energies predicted using ACE, EME-SNAP, POD potentials, while Table 4 shows MAEs in forces. We see that the training errors decrease as the number of descriptors increases. Therefore, the training errors are correlated to the number of descriptors for all potentials. For POD-I and POD-II, the test errors are similar to the training errors. For ACE and EME-SNAP, the test errors in energies are considerably larger than the training errors in energies. In the first four cases, the test errors in forces are similar to the training errors in forces for ACE and EME-SNAP. In the last two cases, the test errors in forces are about two

¹POD-I, POD-II, SNAP, and ACE potentials are available at the Github repository https://github.com/cesmix-mit/pod-examples/tree/main/JCP2023_InP to facilitate the reproduction of this work. The repository contains the input files for training these potentials and the output files for the MAE results reported in Tables 3 and 4. Furthermore, there are input files for running MD simulations with the trained potentials and LAMMPS log files for the computational times reported in Figure 2.

Case	POD-I			POD-II			EME-SNAP		
	N_d	r_{\min}	r_{\max}	N_d	r_{\min}	r_{\max}	N_d	J	r_{cut}
1	26	0.30	4.25	134	0.38	4.69	80	1	3.8
2	83	0.31	4.43	731	0.59	4.63	224	2	3.8
3	170	0.56	4.37	2870	0.50	4.76	480	3	3.8
4	314	0.36	4.80	7226	0.62	4.81	880	4	3.8
5	515	0.65	4.93	16355	0.72	4.91	1456	5	3.8
6	764	0.65	4.93	–	–	–	2240	6	3.8
7	1058	0.65	4.93	–	–	–	3264	7	3.8

Table 1: The cutoff distances and number of descriptors for EME-SNAP, POD-I, and POD-II. The EME-SNAP potential developed in [42] is used here.

Case	N_d	ℓ_{\max}^1	ℓ_{\max}^2	ℓ_{\max}^3	ℓ_{\max}^4	n_{\max}^1	n_{\max}^2	n_{\max}^3	n_{\max}^4
1	70	1	1	1	0	2	2	1	0
2	252	1	2	3	0	8	3	1	0
3	446	1	2	4	0	16	4	1	0
4	738	1	3	5	0	12	5	1	0
5	1190	1	4	6	0	8	6	2	0
6	3496	1	4	6	1	8	6	2	1
7	6046	1	4	6	2	8	6	2	2

Table 2: The number of descriptors, angular degrees, and radial degrees for ACE potentials. Here ℓ_{\max}^r and n_{\max}^r refer to the maximum polynomial of degree of spherical harmonics and radial basis functions for the $(r + 1)$ -body descriptors, respectively. For all cases, the outer cut-off radii are $r_{\max}^{\text{InIn}} = 5.790$, $r_{\max}^{\text{InP}} = 5.007$, $r_{\max}^{\text{PP}} = 4.224$, while the inner cut-off radii are $r_{\min}^{\text{InIn}} = 1.705$, $r_{\min}^{\text{InP}} = 1.403$, $r_{\min}^{\text{PP}} = 1.100$. The ACE potentials are trained by using the FitSNAP package [46] and the ML-PACE package [47].

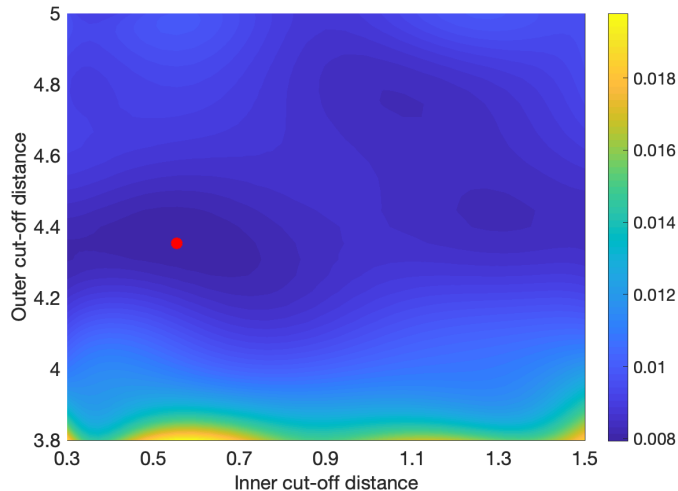


Figure 1: Surrogate loss function of the POD-I potential as a function of inner and outer cutoff distances for $N_d = 170$. The red circle indicates the optimal value of the cutoff distances for which the surrogate loss function is minimum

times greater than the training errors in forces for ACE and EME-SNAP. The training errors for ACE are smaller than the training errors for POD-I, whereas the test errors for ACE are larger than the test errors for POD-I. We observe that POD-II has significantly lower errors than the other potentials.

Case	ACE		POD-I		POD-II		EME-SNAP	
	training	test	training	test	training	test	training	test
1	27.05	99.72	21.18	18.78	4.08	3.90	64.75	160.15
2	3.17	11.58	4.13	4.25	0.95	0.96	10.01	49.32
3	1.66	12.02	2.88	2.82	0.38	0.40	3.16	29.64
4	1.26	9.76	1.61	1.63	0.17	0.24	1.45	15.51
5	0.90	7.73	1.01	1.02	0.07	0.40	0.47	9.46
6	0.67	17.77	0.57	0.61	–	–	0.32	19.48
7	0.65	8.29	0.34	0.39	–	–	0.22	47.07

Table 3: Mean absolute errors (MAEs) in energies for ACE, EME-SNAP, POD-I, POD-II potentials. The unit of MAEs in energies is meV/atom.

Figure 2 shows the trade-off between computational cost and force errors for cases listed in Table 1. The computational cost is measured in terms of number of cores multiplied by the run time in seconds per time steps per atoms for molecular dynamics (MD) simulations. These MD simulations are

Case	ACE		POD-I		POD-II		EME-SNAP	
	training	test	training	test	training	test	training	test
1	77.51	79.19	62.65	57.88	32.70	31.48	261.77	265.46
2	19.18	17.58	36.20	35.73	14.63	14.63	104.15	103.62
3	15.82	17.74	24.18	25.72	7.15	7.01	68.03	76.44
4	14.47	18.15	20.11	23.22	3.92	3.91	32.04	44.15
5	12.72	18.31	15.21	15.83	2.27	2.33	16.89	30.39
6	8.25	16.11	12.41	12.13	–	–	12.74	25.42
7	7.85	15.47	10.19	9.89	–	–	7.90	21.44

Table 4: Mean absolute errors (MAEs) in forces for ACE, EME-SNAP, POD-I, POD-II potentials. The unit of MAEs in forces is meV/Å.

performed using LAMMPS [48] on the 2.1 GHz Intel Broadwell E5-2695 v4 2S x 18C processor of 36 cores with $10 \times 10 \times 10$ bulk supercell containing 8000 InP atoms. We see that POD-II has the same computational cost as POD-I, while having considerably lower force errors than POD-I. This is because POD-II has a greater number of descriptors than POD-I for exactly the same computational complexity. Meanwhile, ACE, POD-I, and POD-II are many times faster than EME-SNAP for the same accuracy. For the level of accuracy of force errors less than $0.015 \text{ eV}/\text{Å}$, POD-II outperforms the other potentials in the sense that POD-II has the lowest computational cost for such level of accuracy. However, ACE performs better than POD-II for the accuracy of force errors of more than $0.015 \text{ eV}/\text{Å}$.

Due to the quadratic per-atom descriptors, the quadratic POD potential demonstrates significantly greater accuracy compared to the linear POD, SNAP, and ACE potentials. This enhanced accuracy largely stems from the global scope of the quadratic per-atom descriptors, which take into account the entire system rather than just local interactions. This global approach allows for a more detailed and accurate modeling of complex atomic behaviors and interactions. In contrast, because the linear POD, SNAP, and ACE potentials are short-range potentials, they may not be able to capture important global effects. This limitation highlights the advantage of the quadratic POD potential in environments where long-range interactions play a critical role in the behavior of the system.

Figure 3 displays the histogram of mean absolute energy errors for all the training structures as predicted by POD-I and POD-II for Case 3. For POD-I, more than 50% of the structures has an energy error of less than 2

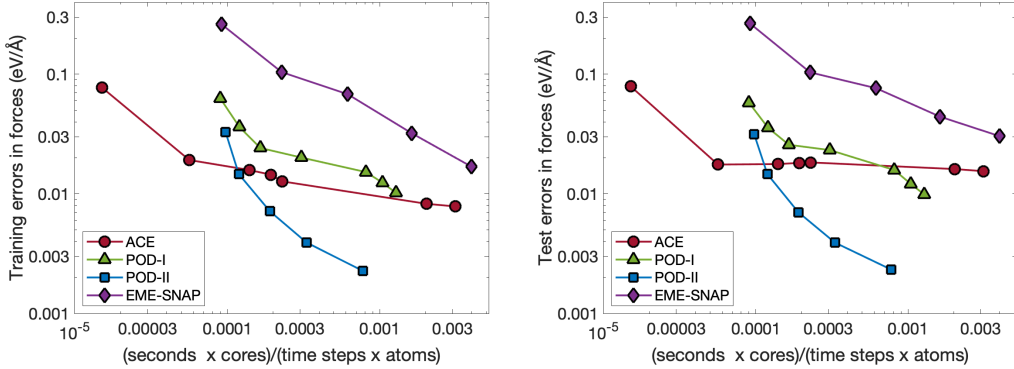


Figure 2: Force errors versus the computational cost of MD simulations for the InP system of 8000 atoms. MD simulations are performed using LAMMPS [48] on the 2.1 GHz Intel Broadwell E5-2695 v4 2S x 18C of 36 cores for ACE, EME-SNAP, POD-I, POD-II for the cases listed in Table 1.

meV/atom, while 99% of the structures are predicted with an energy error of less than 10 meV/atom. For POD-II, almost all the structures are predicted with an energy error of less than 1 meV/atom, while 75% of the structures has an energy error of less than 0.2 meV/atom. Although these error statistics for energy prediction are very good, for practical purposes it is crucial that atomic forces are predicted accurately. No matter how accurate the energy prediction is, the potential is unsuitable for molecular dynamics simulations if the predicted forces are inaccurate. As shown in Figure 4, more than 95% of the structures are predicted with a force error of less than 80 meV/Å for POD-I and 20 meV/Å for POD-II. At such level of accuracy in force prediction, POD-I is acceptable for molecular dynamics simulations, while POD-II is far superior to POD-I.

Point defects are created when atoms become vacant at lattice sites (vacancy defect), occupy locations in the crystal structure at which there are usually not an atom (interstitial defect), or exchange positions with other atoms of different types (antisite defect). Table 5 (respectively, Table 6) shows the errors in energies (respectively, forces) for the following point defects created from an equilibrium configuration of 64 atoms: In_aP_a , In_vP_v , In_a , P_a , In_i , P_i , In_v , and P_v , where subscripts correspond to vacancy(v), interstitial(i) and anti-site(a) defects. All the potentials predict these point defects very accurately. EME-SNAP predicts the vacancy defects more accurately than the other point defects. POD-II has the lowest errors for almost

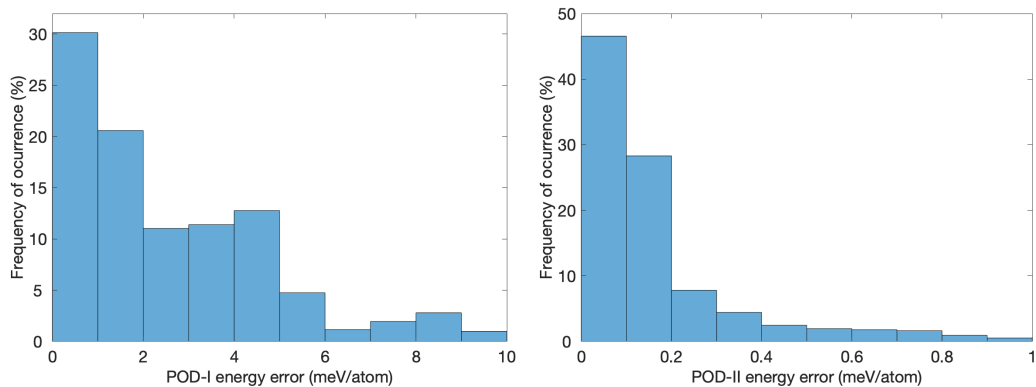


Figure 3: Histogram distribution of energy errors for all structures in the training set as predicted by POD-I (left) and POD-II (right) for Case 3.

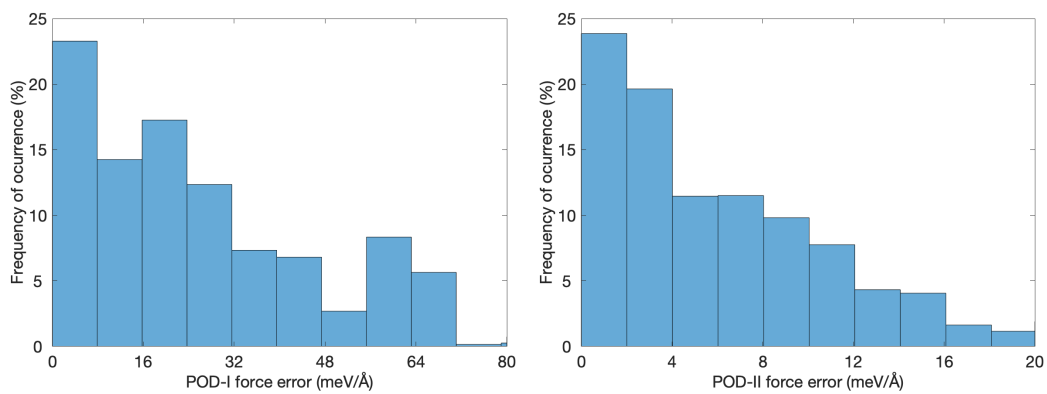


Figure 4: Histogram distribution of force errors for all structures in the training set as predicted by POD-I (left) and POD-II (right) for Case 3.

point defects.

Defect Type		ACE		POD-I		POD-II		EME-SNAP	
Name	N_{atom}	train	test	train	test	train	test	train	test
In_aP_a	64	0.32	0.43	6.84	6.89	0.03	0.02	0.02	0.06
In_vP_v	62	4.78	3.86	2.15	2.52	0.02	0.01	0.04	0.05
In_a	64	0.61	0.92	1.45	1.41	0.12	0.13	0.15	0.25
P_a	64	1.31	0.89	3.30	3.36	0.08	0.13	0.59	8.69
In_i	65	0.61	0.70	0.66	0.59	0.02	0.02	0.06	0.22
P_i	65	0.97	2.97	0.53	0.50	0.02	0.02	0.24	1.00
In_v	63	0.08	0.17	3.80	3.72	0.03	0.02	0.03	0.02
P_v	63	3.40	5.33	0.27	0.24	0.03	0.04	0.03	0.02

Table 5: MAEs in energies (meV/atom) for different point defects for ACE, EME-SNAP, POD-I, POD-II potentials with Case 5. The point defects are created from an equilibrium configuration of 64 atoms by inserting atoms (interstitial defects), removing atoms (vacancy defects), or exchanging atoms of different types (antisite defects). Subscripts correspond to vacancy(v), interstitial(i) and antisite(a) point defects.

Defect Type		ACE		POD-I		POD-II		EME-SNAP	
Name	N_{atom}	train	test	train	test	train	test	train	test
In_aP_a	64	9.93	9.49	24.07	23.87	2.47	2.01	13.24	12.14
In_vP_v	62	25.03	24.48	34.36	40.90	2.97	2.99	7.15	13.86
In_a	64	14.29	14.13	9.93	10.72	1.58	1.64	32.46	32.82
P_a	64	15.54	21.57	26.42	29.69	2.30	2.49	24.51	85.14
In_i	65	13.24	38.37	28.46	28.47	2.44	2.37	16.20	68.10
P_i	65	19.74	32.95	21.84	21.56	2.21	2.20	16.18	39.11
In_v	63	8.50	7.82	17.41	15.85	1.78	2.00	0.45	0.93
P_v	63	11.76	11.19	18.08	14.56	1.67	1.44	2.38	2.36

Table 6: MAEs in forces (meV/Å) for different point defects for ACE, EME-SNAP, POD-I, POD-II potentials with Case 5.

In addition to defect formation energies, we also study cohesive energies for different low-energy crystal structures. Figure 5 plots the energy per atom computed with DFT, POD-I, POD-II as a function of volume per atom for the rocksalt (RS) and zincblende (ZB) crystal structures. We see that the predicted cohesive energies are very close to the DFT cohesive energies for both the rocksalt (RS) and zincblende (ZB) crystal structures. Furthermore, POD-I and POD-II correctly predict ZB as the most stable structure and

reproduce the experimental cohesive energy of -3.48 eV/atom at a volume of $24.4 \text{ \AA}^3/\text{atom}$ [49]. The predicted cohesive energies for the RS structure match exactly the DFT value of -3.30 eV/atom at a volume of $19.7 \text{ \AA}^3/\text{atom}$. While not plotted in Figure 5, the predicted cohesive energies for the wurtzite ground state structure agree well with the DFT value of -3.45 eV/atom at a volume of $25.1 \text{ \AA}^3/\text{atom}$. The potentials accurately predict the cohesive energies for the low-energy crystal structures.

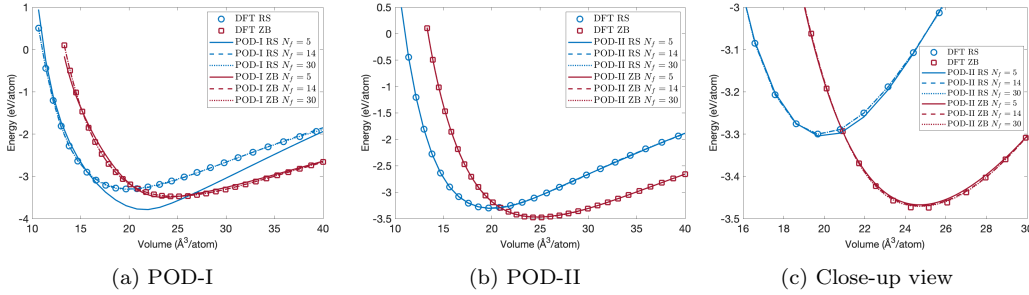


Figure 5: Energy per atom versus volume per atom for rocksalt (RS) and zincblende (ZB) crystal structures of the InP compound for POD-I and POD-II potentials. The right figure shows the close-up view of the curves near the cohesive energies. Here $N_f = N_b^{(2)} + N_b^{(3)}$ is the total number of basis functions for POD potentials.

In this study, the point defects of the InP compound were the primary focus, since accurately reproducing the defect formation energies is essential for realistic simulations of radiation damage [42]. We found that the quadratic POD potential significantly improves the accuracy of energy and force predictions when it is compared to the linear POD potential as well as ACE and EME-SNAP potentials. Specifically, it has approximately 10 smaller energy errors and 4 times smaller force errors than the linear POD potential. We also found that all the potentials are able to accurately predict the formation energies of many different defects far beyond the chemical accuracy of DFT. Nevertheless, additional training data will be needed to improve these ML potentials for other target applications. For instance, adding liquid phase training data is useful to study melting of InP.

5.2. Titanium dioxide

Titanium dioxide (TiO_2) is one of the most chemically stable, environmentally compatible, and functionally versatile metal oxides, thereby making itself an ideal compound to demonstrate interatomic potentials. Over the

years, several empirical potentials have been developed for TiO_2 , including rigid-ion models [50, 51], polarizable models [52, 53], ReaxFF potential [54], and COMB potential [55]. More recently, a number of neural network potentials have been constructed for TiO_2 , including artificial neural network (ANN) potential [56], committee neural network (CNN) potential [57], and deep neural network (DNN) potential [58]. Herein we would like to demonstrate the performance of ACE, SNAP, and POD potentials for TiO_2 on publicly available DFT data set [56].

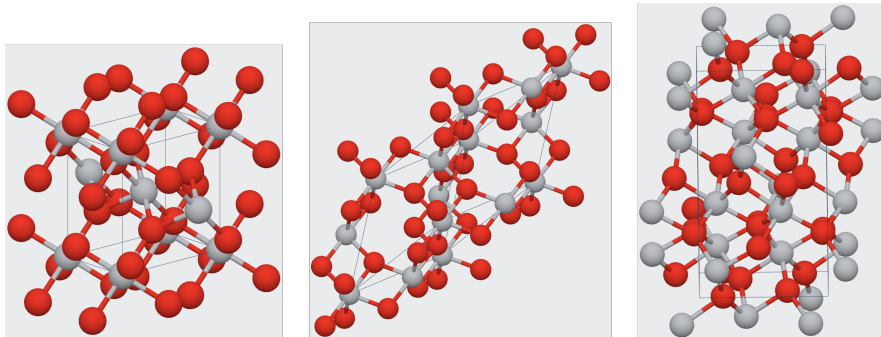


Figure 6: Unit cells of the three TiO_2 polymorphs: rutile (left), anatase (middle), and (c) brookite (right). Red spheres indicate oxygen atoms and grey spheres are titanium atoms.

Natural TiO_2 minerals occur in three polymorphs: rutile (tetragonal), anatase (tetragonal), and brookite (orthorhombic). The unit cells of these polymorphs are shown in Figure 6. In [56], a diverse DFT data set was generated to train an ANN potential for TiO_2 using an iterative refinement method. An initial set of reference structures was generated by distorting ideal rutile, anatase, and brookite structures around the ground state. In addition, supercell structures with oxygen vacancies were also included in the initial data set. Subsequently, additional reference structures were generated by performing short molecular dynamics simulations at various temperatures. This process was repeated until the newly generated structures were found to be accurately represented by the ANN potential. The final data set comprised a total of 7815 structures containing between 6 and 95 atoms. We refer to [56] for additional information about the DFT data set for TiO_2 .

We use 50% of the data set (3908 training structures) to fit ACE, SNAP, and POD potentials, while employing the rest of the data set (3907 test structures) as an independent testing set to assess the accuracy of the potentials and detect overfitting. A common way to detect overfitting is to compare the

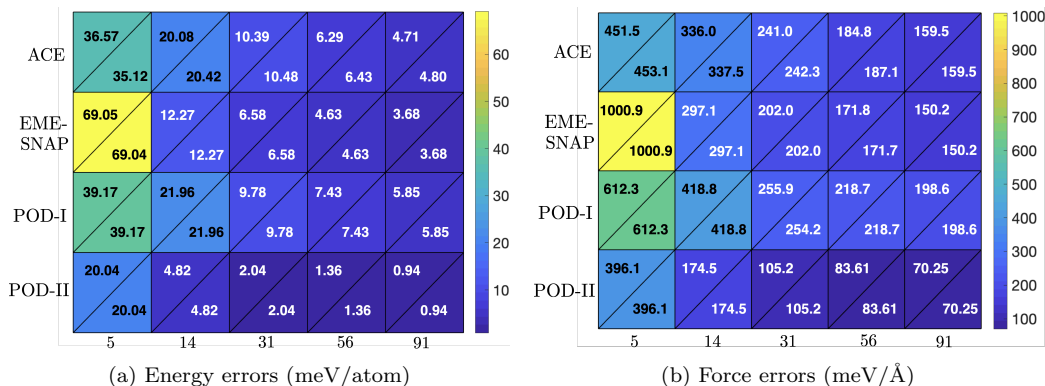


Figure 7: Mean absolute errors in energies (a) and forces (b) for $N_f = 5, 14, 31, 56, 91$ for TiO_2 . The upper left and lower right triangles within each cell represent training and test errors, respectively. For POD potentials, the number of basis functions N_f is defined as the sum of the two-body and three-body basis functions. For ACE and EME-SNAP, the number of basis functions N_f is defined as the number of bispectrum components per atom for one-element systems.

accuracy of the model for test structures (test errors) to the accuracy of the model for training structures (training errors). The training and test errors are shown in Figure 7. The test errors are almost identical to the training errors for ACE, SNAP, and POD-I, POD-II potentials. The convergence of both energy and force errors is quite fast when N_f is less than 30. The errors decrease quite slowly as N_f increases above 30. In terms of accuracy comparison, ACE is slightly more accurate than POD-I, while SNAP is more accurate than ACE. POD-II is the most accurate potential since it has the lowest energy and force errors. Indeed, POD-II with $N_f = 30$ is even more accurate than POD-I, ACE and SNAP with $N_f = 91$. For $N_f = 91$, POD-II predicts the mean absolute errors of about 0.94 meV/atom and 70 meV/Å which are several times smaller than those predicted by the other potentials.

We emphasize that while we compare our approach to the linear ACE and SNAP potentials, it is conceivable that a nonlinear ACE potential [47] or an equivariant message passing neural network potential like MACE [59] may offer comparable improvements. Further exploration into these potentials could provide additional insights into the effectiveness of different computational approaches for modeling complex interactions within systems.

Figure 8 displays the histogram of mean absolute energy errors for all the test structures as predicted by POD-I and POD-II using $N_f = 30$ basis functions. For POD-I, more than 55% of the structures has an energy error

of less than 8 meV/atom, while 99% of the structures are predicted with an energy error of less than 50 meV/atom. For POD-II, almost all the structures are predicted with an energy error of less than 12 meV/atom, while 55% of the structures has an energy error of less than 2 meV/atom. The errors predicted by POD-II are several times less than those by POD-I. Hence, POD-II provides significantly more accurate prediction than POD-I while having the same computational cost.

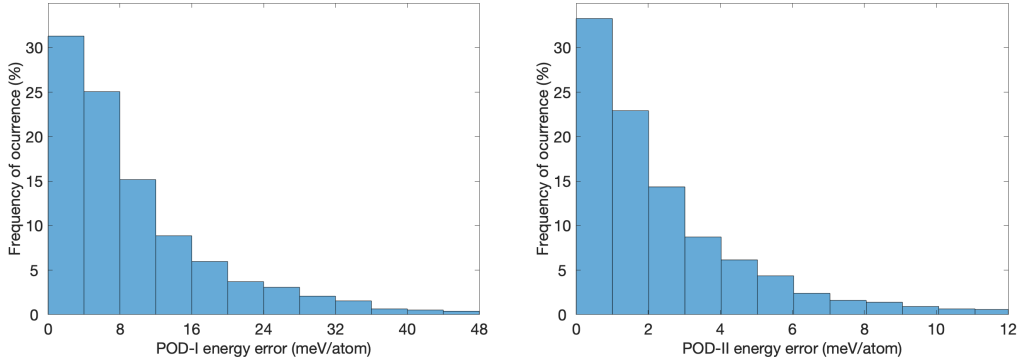


Figure 8: Histogram distribution of energy errors for all structures in the test set as predicted by POD-I (left) and POD-II (right) using $N_f = 30$ basis functions.

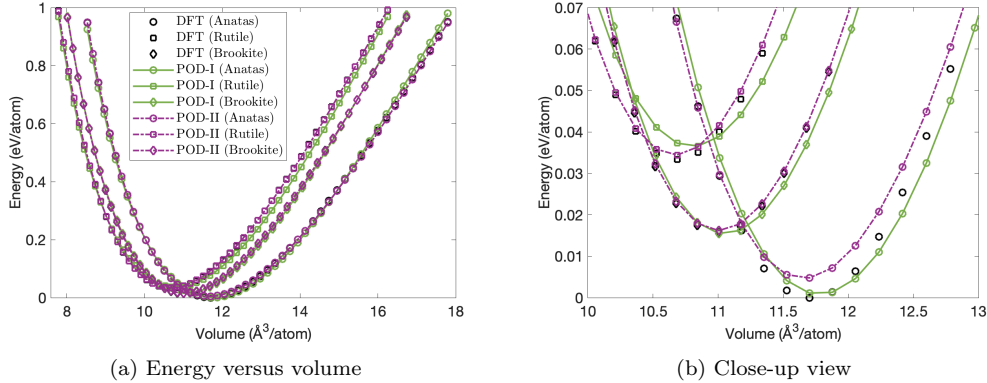


Figure 9: Energy per atom versus volume per atom for anatase, rutile, and brookite crystal structures of the TiO_2 compound for DFT, and POD-I, POD-II potentials with $N_f = 30$. The right figure shows the close-up view of the curves near the cohesive energies.

Figure 9 plots the energy per atom computed with DFT, POD-I, and POD-II as a function of volume per atom for the anatase, rutile, and brookite

crystal structures. Both POD-I and POD-II potentials smoothly reproduce the energy as function of the lattice volume of rutile, anatase, and brookite. It is crucial that the energies of similar structures are reproduced smoothly. If the energy errors on the order of 2 meV/atom were completely stochastic, the potential energy surface would be rugged and thus unsuitable for MD simulations. Table 7 summarizes the cohesive energies and unit cell volumes for the rutile, anatase, and brookite structures. The agreement between the values predicted by the POD potentials and their DFT references is excellent.

Crystal phase	DFT		POD-I		POD-II	
	E_0	V_0	E_0	V_0	E_0	V_0
Anatase	0.000	11.71	0.001	10.70	0.005	10.70
Rutile	0.033	10.68	0.037	10.85	0.034	10.68
Brookite	0.016	11.01	0.016	11.01	0.016	11.01

Table 7: Cohesive energies per atom E_0 (eV/atom) and unit cell volumes per atom V_0 ($\text{\AA}^3/\text{atom}$) for three different TiO_2 phases as computed using density-functional theory (DFT) and POD potentials with $N_f = 30$.

In this study, the phase energies of the TiO_2 compound were the primary focus, since smoothly reproducing the phase energies is essential for MD simulations. The quadratic POD potential provided more accurate predictions than the other potentials. The reference data set was restricted to periodic bulk structures. As a consequence, the constructed TiO_2 potentials can therefore not be expected to describe surface models (slab structures) or liquid phase accurately. Additional training data will be needed to further improve these potentials for other target applications.

6. Conclusions

We have developed proper orthogonal descriptors for multi-element chemical systems based on the orthogonal expansion of the radial and angular components of the parametrized potentials. In our work, the parametrized potentials are designed to provide a rich and diverse representation of two-body and three-body interactions. We compose the proper orthogonal descriptors in two different ways to construct two different interatomic potentials. The first POD potential expresses the energy of each atom as a linear combination of proper orthogonal descriptors, while the second POD potential expresses the energy as a linear and quadratic combination of the descriptors.

We have demonstrated the two POD potentials for indium phosphide and titanium dioxide, and compared their performance to that of multi-element SNAP and ACE potentials. For all potentials, increasing the number of basis functions usually improves prediction of energies and forces. The quadratic POD potential was shown to provide much more accurate prediction of energies and forces than the linear POD potential at the same computational cost. The improvement stems from the composition of two-body and three-body descriptors to construct four-body descriptors without increasing the computational complexity of the resulting potential.

The ideas presented in this paper can be extended to both empirical and machine learning potentials. Recently, a more efficient form of the proper orthogonal descriptors is developed by employing the atom density formulation [31]. We would like to extend the work [31] to multi-element chemical systems by utilizing the presented ideas. The two-body orthogonal basis functions developed herein can be used as radial basis functions in power spectrum, bispectrum, SOAP and ACE descriptors. Instead of fitting the parameters of empirical potentials, one can use the present method to construct an orthogonal basis for the parametric manifold of empirical potentials. This approach may improve the accuracy and transferability of existing empirical potentials.

Acknowledgements

I am grateful to Dr. Andrew Rohskopf at Sandia National Laboratories (SNL) for fitting ACE potentials and running MD simulations. I would like to thank all members of the CESMIX center at MIT for fruitful and invaluable discussions leading me to the ideas presented in this work. I would like to thank Dr. Axel Kohlmeyer at Temple University and Dr. Aidan Thompson (SNL) for fruitful discussions about LAMMPS implementation of POD potentials. I would also like to thank the reviewers for their constructive comments. I gratefully acknowledge the United States Department of Energy under contract DE-NA0003965 and the Air Force Office of Scientific Research under Grant No. FA9550-22-1-0356 for supporting this work.

References

- [1] M. S. Daw, M. I. Baskes, Embedded-atom method: Derivation and application to impurities, surfaces, and other defects in metals, *Physical Review B* 29 (12) (1984) 6443–6453. doi:10.1103/PhysRevB.29.6443.

- [2] F. H. Stillinger, T. A. Weber, Computer simulation of local order in condensed phases of silicon, *Physical Review B* 31 (8) (1985) 5262–5271. doi:10.1103/PhysRevB.31.5262.
- [3] J. Tersoff, New empirical approach for the structure and energy of covalent systems, *Physical Review B* 37 (12) (1988) 6991–7000. doi:10.1103/PhysRevB.37.6991.
- [4] M. Z. Bazant, E. Kaxiras, J. Justo, Environment-dependent interatomic potential for bulk silicon, *Physical Review B - Condensed Matter and Materials Physics* 56 (14) (1997) 8542–8552. arXiv:9704137, doi:10.1103/PhysRevB.56.8542.
- [5] D. W. Brenner, O. A. Shenderova, J. A. Harrison, S. J. Stuart, B. Ni, S. B. Sinnott, A second-generation reactive empirical bond order (REBO) potential energy expression for hydrocarbons, *Journal of Physics Condensed Matter* 14 (4) (2002) 783–802. doi:10.1088/0953-8984/14/4/312.
- [6] A. C. Van Duin, S. Dasgupta, F. Lorant, W. A. Goddard, ReaxFF: A reactive force field for hydrocarbons, *Journal of Physical Chemistry A* 105 (41) (2001) 9396–9409. doi:10.1021/jp004368u.
- [7] A. P. Bartók, R. Kondor, G. Csányi, On representing chemical environments, *Physical Review B - Condensed Matter and Materials Physics* 87 (18) (2013). arXiv:1209.3140, doi:10.1103/PhysRevB.87.184115.
- [8] J. Behler, Perspective: Machine learning potentials for atomistic simulations, *Journal of Chemical Physics* 145 (17) (2016) 170901. doi:10.1063/1.4966192.
- [9] G. Dusson, M. Bachmayr, G. Csányi, R. Drautz, S. Etter, C. van der Oord, C. Ortner, Atomic cluster expansion: Completeness, efficiency and stability, *Journal of Computational Physics* 454 (2022) 110946. arXiv:1911.03550, doi:10.1016/j.jcp.2022.110946.
URL <https://www.sciencedirect.com/science/article/pii/S0021999122000080>
- [10] J. Behler, M. Parrinello, Generalized neural-network representation of high-dimensional potential-energy surfaces, *Physical Review Letters* 98 (14) (2007). doi:10.1103/PhysRevLett.98.146401.

- [11] J. Behler, Atom-centered symmetry functions for constructing high-dimensional neural network potentials, *Journal of Chemical Physics* 134 (7) (2011). doi:10.1063/1.3553717.
- [12] J. Behler, Representing potential energy surfaces by high-dimensional neural network potentials, *Journal of Physics Condensed Matter* 26 (18) (2014). doi:10.1088/0953-8984/26/18/183001.
- [13] A. P. Bartók, M. C. Payne, R. Kondor, G. Csányi, Gaussian approximation potentials: The accuracy of quantum mechanics, without the electrons, *Physical Review Letters* 104 (13) (2010). arXiv:0910.1019, doi:10.1103/PhysRevLett.104.136403.
- [14] S. Fujikake, V. L. Deringer, T. H. Lee, M. Krynski, S. R. Elliott, G. Csányi, Gaussian approximation potential modeling of lithium intercalation in carbon nanostructures, *Journal of Chemical Physics* 148 (24) (2018). arXiv:1712.04472, doi:10.1063/1.5016317.
- [15] W. J. Szlachta, A. P. Bartók, G. Csányi, Accuracy and transferability of Gaussian approximation potential models for tungsten, *Physical Review B - Condensed Matter and Materials Physics* 90 (10) (2014). doi:10.1103/PhysRevB.90.104108.
- [16] A. P. Thompson, L. P. Swiler, C. R. Trott, S. M. Foiles, G. J. Tucker, Spectral neighbor analysis method for automated generation of quantum-accurate interatomic potentials, *Journal of Computational Physics* 285 (2015) 316–330. doi:10.1016/j.jcp.2014.12.018.
- [17] M. A. Wood, A. P. Thompson, Extending the accuracy of the SNAP interatomic potential form, *Journal of Chemical Physics* 148 (24) (2018) 241721. arXiv:1711.11131, doi:10.1063/1.5017641.
- [18] I. I. Novoselov, A. V. Yanilkin, A. V. Shapeev, E. V. Podryabinkin, Moment tensor potentials as a promising tool to study diffusion processes, *Computational Materials Science* 164 (2019) 46–56. arXiv:1812.02946, doi:10.1016/j.commatsci.2019.03.049.
- [19] A. V. Shapeev, Moment tensor potentials: A class of systematically improvable interatomic potentials, *Multiscale Modeling and Simulation* 14 (3) (2016) 1153–1173. arXiv:1512.06054, doi:10.1137/15M1054183.

- [20] R. Drautz, Atomic cluster expansion for accurate and transferable interatomic potentials, *Physical Review B* 99 (1) (2019). doi:10.1103/PhysRevB.99.014104.
- [21] R. Drautz, Atomic cluster expansion of scalar, vectorial, and tensorial properties including magnetism and charge transfer, *Physical Review B* 102 (2) (2020). arXiv:2003.00221, doi:10.1103/PhysRevB.102.024104.
- [22] Y. Zuo, C. Chen, X. Li, Z. Deng, Y. Chen, J. Behler, G. Csányi, A. V. Shapeev, A. P. Thompson, M. A. Wood, S. P. Ong, Performance and Cost Assessment of Machine Learning Interatomic Potentials, *Journal of Physical Chemistry A* 124 (4) (2020) 731–745. arXiv:1906.08888, doi:10.1021/acs.jpca.9b08723.
- [23] N. C. Nguyen, A. Rohskopf, Proper orthogonal descriptors for efficient and accurate interatomic potentials, *Journal of Computational Physics* 480 (2023) 112030. doi:https://doi.org/10.1016/j.jcp.2023.112030.
URL <https://www.sciencedirect.com/science/article/pii/S0021999123001250>
- [24] M. Barrault, Y. Maday, N. C. Nguyen, A. T. Patera, An 'empirical interpolation' method: application to efficient reduced-basis discretization of partial differential equations, *Comptes Rendus Mathématique* 339 (9) (2004) 667–672. doi:10.1016/J.Crma.2004.08.006.
URL <http://www.sciencedirect.com/science/article/pii/S1631073X04004248>
- [25] S. Boyaval, C. L. Bris, Y. Maday, N. C. Nguyen, A. T. Patera, A reduced basis approach for variational problems with stochastic parameters: Application to heat conduction with variable Robin coefficient, *Computer Methods in Applied Mechanics and Engineering* 198 (41-44) (2009) 3187–3206. doi:10.1016/j.cma.2009.05.019.
URL <http://linkinghub.elsevier.com/retrieve/pii/S0045782509002114>
- [26] M. A. Grepl, Y. Maday, N. C. Nguyen, A. T. Patera, Efficient reduced-basis treatment of nonaffine and nonlinear partial differential equations, *Mathematical Modelling and Numerical Analysis* 41 (3) (2007) 575–605.

doi:10.1051/m2an:2007031.

URL <http://www.esaim-m2an.org/10.1051/m2an:2007031>

- [27] G. Rozza, D. B. P. Huynh, A. T. Patera, Reduced basis approximation and a posteriori error estimation for affinely parametrized elliptic coercive partial differential equations: Application to transport and continuum mechanics, *Archives Computational Methods in Engineering* 15 (4) (2008) 229–275.
- [28] N. C. Nguyen, A multiscale reduced-basis method for parametrized elliptic partial differential equations with multiple scales, *Journal of Computational Physics* 227 (23) (2008) 9807–9822.
URL <http://www.scopus.com/inward/record.url?eid=2-s2.0-53349103005&partnerID=40&md5=64852a2fac4b34c956379f980e2cf264>
- [29] N. C. Nguyen, J. Peraire, Efficient and accurate nonlinear model reduction via first-order empirical interpolation, *Journal of Computational Physics* 494 (2023) 112512. arXiv:2305.00466, doi:10.1016/j.jcp.2023.112512.
URL <http://arxiv.org/abs/2305.00466>
- [30] A. Rohskopf, J. Goff, D. Sema, K. Gordiz, N. C. Nguyen, A. Henry, A. P. Thompson, M. A. Wood, Exploring model complexity in machine learned potentials for simulated properties, *Journal of Materials Research* 38 (24) (2023) 5136–5150. arXiv:2306.02255, doi:10.1557/s43578-023-01152-0.
- [31] N. C. Nguyen, Fast proper orthogonal descriptors for many-body interatomic potentials, *Physical Review B* 107 (14) (2023) 144103. arXiv:2212.14446, doi:10.1103/PhysRevB.107.144103.
URL <http://arxiv.org/abs/2212.14446>
- [32] N. Artrith, A. Urban, G. Ceder, Efficient and accurate machine-learning interpolation of atomic energies in compositions with many species, *Physical Review B* 96 (1) (2017). arXiv:1706.06293, doi:10.1103/PhysRevB.96.014112.
- [33] M. Gastegger, L. Schwiedrzik, M. Bittermann, F. Berzsényi, P. Marquetand, WACSF - Weighted atom-centered symmetry functions as de-

- scriptors in machine learning potentials, *Journal of Chemical Physics* 148 (24) (2018). [arXiv:1712.05861](#), [doi:10.1063/1.5019667](#).
- [34] M. J. Willatt, F. Musil, M. Ceriotti, Feature optimization for atomistic machine learning yields a data-driven construction of the periodic table of the elements, *Physical Chemistry Chemical Physics* 20 (47) (2018) 29661–29668. [arXiv:1807.00236](#), [doi:10.1039/c8cp05921g](#).
- [35] K. Gubaev, E. V. Podryabinkin, G. L. Hart, A. V. Shapeev, Accelerating high-throughput searches for new alloys with active learning of interatomic potentials, *Computational Materials Science* 156 (2019) 148–156. [arXiv:1806.10567](#), [doi:10.1016/j.commatsci.2018.09.031](#).
- [36] J. P. Darby, J. R. Kermode, G. Csányi, Compressing local atomic neighbourhood descriptors, *npj Computational Materials* 8 (1) (2022). [arXiv:2112.13055](#), [doi:10.1038/s41524-022-00847-y](#).
- [37] T. Kostiuhenko, F. Körmann, J. Neugebauer, A. Shapeev, Impact of lattice relaxations on phase transitions in a high-entropy alloy studied by machine-learning potentials, *npj Computational Materials* 5 (1) (2019). [arXiv:1810.10820](#), [doi:10.1038/s41524-019-0195-y](#).
- [38] J. P. Darby, D. P. Kovács, I. Batatia, M. A. Caro, G. L. W. Hart, C. Ortner, G. Csányi, Tensor-reduced atomic density representations, *arXiv preprint arXiv:2210.01705* (2022).
- [39] J. Nigam, S. Pozdnyakov, M. Ceriotti, Recursive evaluation and iterative contraction of N -body equivariant features, *Journal of Chemical Physics* 153 (12) (2020). [arXiv:2007.03407](#), [doi:10.1063/5.0021116](#).
- [40] A. Goscinski, F. Musil, S. Pozdnyakov, J. Nigam, M. Ceriotti, Optimal radial basis for density-based atomic representations, *Journal of Chemical Physics* 155 (10) (2021). [arXiv:2105.08717](#), [doi:10.1063/5.0057229](#).
- [41] C. Zeni, K. Rossi, A. Glielmo, S. De Gironcoli, Compact atomic descriptors enable accurate predictions via linear models, *Journal of Chemical Physics* 154 (22) (2021). [arXiv:2105.11231](#), [doi:10.1063/5.0052961](#).
- [42] M. A. Cusentino, M. A. Wood, A. P. Thompson, Explicit Multielement Extension of the Spectral Neighbor Analysis Potential for Chemically

- Complex Systems, *The Journal of Physical Chemistry A* 124 (26) (2020) 5456–5464. doi:10.1021/acs.jpca.0c02450.
URL <https://doi.org/10.1021/acs.jpca.0c02450>
- [43] L. Sirovich, Turbulence and the Dynamics of Coherent Structures, Part 1: Coherent Structures, *Quarterly of Applied Mathematics* 45 (3) (1987) 561–571.
- [44] K. Willcox, J. Peraire, Balanced Model Reduction via the Proper Orthogonal Decomposition, *AIAA* 40 (11) (2002) 2323.
- [45] N. C. Nguyen, A. T. Patera, J. Peraire, A 'best points' interpolation method for efficient approximation of parametrized functions, *International Journal for Numerical Methods in Engineering* 73 (4) (2008) 521–543. doi:10.1002/nme.2086.
URL <http://doi.wiley.com/10.1002/nme.2086>
- [46] A. Rohskopf, C. Sievers, N. Lubbers, M. A. Cusentino, J. Goff, J. Janssen, M. McCarthy, D. M. O. de Zapiain, S. Nikolov, K. Sargsyan, Others, FitSNAP: Atomistic machine learning with LAMMPS, *Journal of Open Source Software* 8 (84) (2023) 5118.
- [47] Y. Lysogorskiy, C. van der Oord, A. Bochkarev, S. Menon, M. Rinaldi, T. Hammerschmidt, M. Mrovec, A. Thompson, G. Csányi, C. Ortner, R. Drautz, Performant implementation of the atomic cluster expansion (PACE) and application to copper and silicon, *npj Computational Materials* 7 (1) (2021). arXiv:2103.00814, doi:10.1038/s41524-021-00559-9.
- [48] A. P. Thompson, H. M. Aktulga, R. Berger, D. S. Bolintineanu, W. M. Brown, P. S. Crozier, P. J. in 't Veld, A. Kohlmeyer, S. G. Moore, T. D. Nguyen, R. Shan, M. J. Stevens, J. Tranchida, C. Trott, S. J. Plimpton, LAMMPS - a flexible simulation tool for particle-based materials modeling at the atomic, meso, and continuum scales, *Computer Physics Communications* 271 (2022) 108171. doi:10.1016/j.cpc.2021.108171.
- [49] D. N. Nichols, D. S. Rimai, R. J. Sladek, Elastic anharmonicity of InP: Its relationship to the high pressure transition, *Solid State Communications* 36 (8) (1980) 667–669. doi:10.1016/0038-1098(80)90205-7.

- [50] M. Matsui, M. Akaogi, Molecular dynamics simulation of the structural and physical properties of the four polymorphs of TiO_2 , *Molecular Simulation* 6 (4-6) (1991) 239–244. doi:10.1080/08927029108022432.
- [51] P. M. Oliver, G. W. Watson, E. T. Kelsey, S. C. Parker, Atomistic simulation of the surface structure of the TiO_2 polymorphs rutile and anatase, *Journal of Materials Chemistry* 7 (3) (1997) 563–568. doi:10.1039/a606353e.
- [52] V. Swamy, J. D. Gale, Transferable variable-charge interatomic potential for atomistic simulation of titanium oxides, *Physical Review B - Condensed Matter and Materials Physics* 62 (9) (2000) 5406–5412. doi:10.1103/PhysRevB.62.5406.
- [53] V. Swamy, J. D. Gale, L. S. Dubrovinsky, Atomistic simulation of the crystal structures and bulk moduli of TiO_2 polymorphs, *Journal of Physics and Chemistry of Solids* 62 (5) (2001) 887–895. doi:10.1016/S0022-3697(00)00246-8.
- [54] S. Y. Kim, N. Kumar, P. Persson, J. Sofu, A. C. Van Duin, J. D. Kubicki, Development of a ReaxFF reactive force field for titanium dioxide/water systems, *Langmuir* 29 (25) (2013) 7838–7846. doi:10.1021/la4006983.
- [55] Y. T. Cheng, T. R. Shan, T. Liang, R. K. Behera, S. R. Phillpot, S. B. Sinnott, A charge optimized many-body (comb) potential for titanium and titania, *Journal of Physics Condensed Matter* 26 (31) (2014). doi:10.1088/0953-8984/26/31/315007.
- [56] N. Artrith, A. Urban, An implementation of artificial neural-network potentials for atomistic materials simulations: Performance for TiO_2 , *Computational Materials Science* 114 (2016) 135–150. doi:10.1016/j.commatsci.2015.11.047.
- [57] C. Schran, F. L. Thiemann, P. Rowe, E. A. Müller, O. Marsalek, A. Michaelides, Machine learning potentials for complex aqueous systems made simple, *Proceedings of the National Academy of Sciences of the United States of America* 118 (38) (2021). arXiv:2106.00048, doi:10.1073/pnas.2110077118.

- [58] M. F. Andrade, H. Y. Ko, L. Zhang, R. Car, A. Selloni, Free energy of proton transfer at the water-TiO₂ interface from: ab initio deep potential molecular dynamics, *Chemical Science* 11 (9) (2020) 2335–2341. doi:10.1039/c9sc05116c.
- [59] I. Batatia, D. P. Kovács, G. N. Simm, C. Ortner, G. Csányi, MACE: Higher Order Equivariant Message Passing Neural Networks for Fast and Accurate Force Fields, in: *Advances in Neural Information Processing Systems*, Vol. 35, 2022. arXiv:2206.07697.